Structure evolution, bandgap and dielectric function in La-doped hafnium oxide thin layer subjected to swift Xe ion irradiation

E.I. Suvorova[a*], O.V. Uvarov[b], N.A. Arkharova[a], A.D. Ibrayeva[c,d] V.A. Skuratov[e,f,g], P.A. Buffat[h]

[a] A.V. Shubnikov Institute of Crystallography, Federal Scientific Research Centre "Crystallography and Photonics" of Russian Academy of Sciences, Leninsky pr.,59, 119333 Moscow, Russia

[b] Prokhorov General Physics Institute of Russian Academy of Sciences, Vavilov str., 38, 119991 Moscow, Russia

[c] L.N. Gumilyov Eurasian National University, Astana, Kazakhstan

[d] Nur-Sultan Branch of Institute of Nuclear Physics, Nur-Sultan, Kazakhstan

[e] FLNR, JINR, 141980 Dubna, Russia

[f] National Research Nuclear University MEPhI, Kashirskoe shosse, 31, 115409 Moscow, Russia

[g] Dubna State University, Universitetskaja str, 19, 141982 Dubna, Russia

[h] Ecole Polytechnique Fédérale de Lausanne, Centre Interdisciplinaire de Microscopie Electronique, CH-1015, Lausanne, Switzerland

[*] Corresponding author. E-mail address: suvorova@crys.ras.ru

E-mails:

O.V. Uvarov: uvarov@kapella.gpi.ru

N.A. Arkharova: natalya.arkharova@yandex.ru

A.D. Ibrayeva: a.d.ibrayeva@gmail.com

V.A. Skuratov: skuratov@jinr.ru

P.A. Buffat: philippe.buffat@epfl.ch

Abstract

HRTEM, electron diffraction and EELS provide information on the structural evolution, dielectric function, and band gap values of nanocrystalline lanthanum doped hafnia (La:HfO_2) layers 10 nm thick in TiN/La:HfO_2/TiN/SiO_2/Si irradiated with 24, 46, 77 and 160 MeV (0.2 – 1.2 MeV/u) Xe ions. Swift heavy Xe ions were expected to create significant atomic rearrangements when pass through a solid losing energy mainly through electronic excitation and ionization of the target atoms. Local heating and subsequent rapid cooling in the region around the ion track can lead to re-solidification with formation of a new stable crystalline phase, as well direct crystal-to-crystal transformations are possible. The structure evolution of hafnia nanocrystals from orthorhombic *Pbcm* in pristine layer to tetragonal $P4_2/nmc$ phase in 160 MeV Xe ion irradiated layer was observed. The mixture of tetragonal and orthorhombic phases was found in samples irradiated with ions of intermediate energies. Textured hafnia layers were formed as a result of ion irradiation. The changes in plasmon line shape and the blue shift of the plasmon energy loss peak from14.9 eV in pristine layer to 15.4 eV in 46 MeV and 15.9 MeV Xe ion irradiated hafnia reflect structural transformations, the Hf coordination number increase and crystal orientations. Measurements of bandgap with VEELS showed a little change in dielectric function and a slight increase from 6.1 eV in pristine sample to 6.2 eV and 6.3 eV in irradiated samples with 46 and 160 MeV Xe ions, dielectric function changed insignificantly.

Keywords: HfO_2 structure, dielectric function, bandgap, ion irradiation, transmission electron microscopy, electron energy loss spectroscopy.

1. Introduction

Hafnium oxide, HfO_2, can take monoclinic, orthorhombic, tetragonal, and cubic structures. The HfO_2 phase diagram[1] obtained by X-ray diffraction *in situ* at high pressure and high temperature shows phase transformation from $P2_1/c$ monoclinic to high-pressure *Pbca* and *Pmnb* orthorhombic (orthorhombic-I, orthorhombic-II), high-temperature $P4_2/nmc$ tetragonal and *Fm-3m* cubic structures. The less symmetric orthorhombic *Pbcm* phase was not included in this phase diagram, although it was identified and described by Suyama et al.[2] and Adams et al.[3] a few years earlier. A list of HfO_2 phases, their formation conditions and lattice parameters obtained from X-ray or neutron diffraction is presented in Table S1 in Supplementary Materials.

The structural evolution and stabilization of HfO_2 phases with a symmetry higher than monoclinic under normal conditions using dopants Al, Si, Mg, Ca, Ti, Y, Zr, La, Ce, Gd, Dy, Er, Ta in various concentrations has been widely studied[4,5,6] due to importance to improve electrical performance in the device manufacturing[7]. However, for the analyst, assessing the link between electrical properties and structure is challenging due to the close lattice parameters of phases and quite often the structures are assumed and not clearly established in the works.

In addition to doping, swift heavy ions irradiation (SHI) may be used to modify the structure and properties of materials. At present, more information is still needed on local chemical changes and phase transitions, as well as their effect on dielectric properties, and even more in layered structures, for example, HfO_2 layers with a thickness of several nm or tens of nm, grown between thin TiN electrodes. Hafnium-based materials are traditionally regarded as a class of valuable materials in the nuclear industry, for which resistance to phase transitions and external influences is important because of the demands of future applications under extreme conditions. Therefore, we consider that it is important to obtain more experimental results on possible changes occurred in HfO_2 under ion irradiation.

It was reported[8] that some nanocrystalline materials like zirconium nitride layers can exhibit a high degree of resistance against swift heavy ion irradiation in the wide range of fluences and energies. While energy deposition in other materials leads to grain growth[9] or an increase in the isometric unit cell parameter due to the accumulation of defects and, consequently, to material swelling[10].

Structural transformation in monoclinic polycrystalline zirconia irradiated with low energy Xe (340 keV) ions of high fluences (up to $2{\cdot}10^{17}$ cm^{-2}) was reported by Sickafus et al.[11]. Analysis of the electron and X-ray diffraction patterns led them to conclusion that it went to a cubic or tetragonal phase without any traces of an amorphous phase. A local transition towards an amorphous phase was observed in the damaged regions (amorphous tracks) in nanocrystalline yttria buried in a 1-μm thick YBCO layer submitted to swift Kr and Xe ion irradiation with lower fluences[12]. Benyagoub[13,14] observed the appearance of a new diffraction peak at $2\theta \approx 30\text{-}31°$ in X-ray diffraction patterns after irradiation of polycrystalline sintered monoclinic zirconia and hafnia with Ni (135 and 350 MeV) and Kr (300 and 800 MeV) ions and interpreted this observation as a transformation into a cubic or tetragonal phase. The threshold of energy transferred by ion to target electrons (electronic stopping power S_{et}) was determined to be 18.2±0.2 keV/nm. The threshold S_{et} for swift heavy ion irradiation-induced crystallization of hafnia from the amorphous hafnia to the monoclinic phase was found to be about 10 keV/nm[15].

In addition to studies of the irradiation effect on structural changes, another part of the work was devoted to studying the relative permittivity and band gap values of oxides after irradiation. The experimental data obtained for different HfO_2 phases listed in Table 1 shows that the band gap is not very dependent on the structure while larger changes are observed on the relative permittivity although it does not reach the calculated values[16,17]. Some of the differences among the measured properties were explained by the different experimental approaches and/or by the variability in sample preparation[18] and/or film density[20]. While other differences reflect the changes in the

structure of the materials. For instance, the change in bandgap of HfO_2 films 5.78 - 6.17 eV during annealing from 25°C to 700°C corresponds to a phase transition from amorphous to monoclinic[19,21] or morphological and structural features of the hafnia films[36]. It is noteworthy that there are very few experimentally determined values of the band gap for the orthorhombic and cubic phases, and there are still no experimental values for the tetragonal phase. In addition, the computed[17,22] band gap values differ from the experimental ones and are underestimated. Therefore, we believe that it is important to obtain the dielectric constant and bandgap data from the experiment, which in turn helps to improve theoretical models.

Table 1. Experimental values of relative permittivity (static) and band gaps for different HfO_2 phases.

HfO_2 phase	Amorphous	Monoclinic	Orthorhombic	Tetragonal		Cubic	
				pure	doped	pure	doped
Relative permittivity	20 [18, 23] 30 [24]	15-18[23, 25, 28, 32], 22-25[26] 17-20[27, 29]	25-30[30]	35[27] 34[29]	21-28 (Gd, Er, Dy)[28] 25-28 (Si) [23] 35 (Si)[27]	14–22 [30] 30-36 [24] 35-39 [30] 40 [39] 50 [38]	22-29 (Y) [30,32,33] 28 (Yb) [34] 32 (Dy, Sc)[31]
Energy band gap	6.04[24] 5.3–5.8[21,35]	4.3 – 5.25[36] 5.68[26] 6.0[30,38] 5.55[37]	5.9[36]	–	–	6.0 [38] 6.0 [30]	–

Singh et al. [40] investigated the effect of 50 MeV Li^{3+} ion irradiation on HfO_2-based MOS devices and did not establish sufficient clarity for the change in dielectric properties of the hafnia film, but the HfO_2 structure was not identified.

Swift heavy ion irradiation response has been studied in pure HfO_2[13-15,40] with monoclinic or amorphous structure. The goal of the present paper is to study the effect of Xe ion irradiation (0.2 – 1.2 MeV/u energy, $5x10^{11}$ ion·cm^{-2} fluence) on La-doped HfO_2 a few nm thick films which are considered as promising dielectric in microelectronics devices due to a substantially smooth surface, high stability of the La:HfO_2 layer in contact with Si and the quality of the oxide/Si

interface[41]. First, the nature of the phases present in La:HfO_2 thin films embedded between TiN electrodes was determined, and, second, the stability of these phases and possible structural changes induced by irradiation were investigated.

Analytical transmission electron microscopy (TEM), electron diffraction and X-ray energy dispersive spectrometry (EDXS) were applied to obtain chemical, structural, and physical information in a single experiment with a nanometer scale spatial resolution. At that scale, phase identification required high resolution transmission electron microscopy (HRTEM) and interpretation of low loss electron energy loss spectroscopy (EELS) brought band gap estimation and comparative analysis of the dielectric functions.

2. Experimental details

A planar 20nm TiN/10 nm La:HfO_2/20 nm TiN metal-insulator-metal capacitor was deposited on a 150 mm Si wafers coated with a 1 μm thick SiO_2 layer were formed. The La-doped HfO_2 layers was obtained by atomic layer deposition from a $Hf(NC_2H_5CH_3)_4$, $La(i\text{-}C_3H_7C_5H_4)_3$ and O_2 plasma at a 235°C substrate temperature. It was followed by a 650°C annealing. The full details of deposition can be found elsewhere[42].

TiN/La:HfO_2/TiN/SiO_2/Si specimens of 0.5 x 0.5 cm^2 for irradiation were cut from the wafer and mounted on copper water-cooled holders (20°C). Irradiation at room temperature by scanning the ion beam over their whole surface at an average Xe ion flux of 2×10^8 ion·$cm^{-2}s^{-1}$ and fluence of $5x10^{11}$ ion·cm^{-2} was done at the IC-100 FLNR JINR cyclotron facility. Al absorbers of suitable thicknesses were inserted between the Xe ion source and the sample were used to select the energy for irradiation: 160, 72, 46 and 24 MeV (1.2 – 0.2 MeV/u). The electronic stopping power (S_e) of Xe ions, range and changes in the ion energies as they proceed through the successive layers in the conductor wire were calculated using the SRIM2013 (Stopping and Range of Ions in Matter) code[43].

TEM cross-sections from irradiated and pristine samples were thinned with a focused ion beam (FEI Scios FIB) or by conventional Ar ion milling (Gatan PIPS) at room temperature after preliminary mechanical polishing. TEM and STEM images, X-ray EDS microanalysis and electron diffraction patterns were obtained with analytical field emission microscopes at 200 kV accelerating voltage (HV) (FEI Tecnai Osiris) and HV 300 kV (FEI Titan 80-300). The selected area electron diffraction (SAED) patterns and high resolution TEM (HRTEM) images were processed with the DigitalMicrograph GMS 2.31 (Gatan Inc), diffraction patterns and Fourier Transform diffractograms interpreted with the JEMS[44] to derive the phase composition of hafnia layers.

Electron Energy Loss Spectroscopy (EELS) was performed in a Libra 200 FE HR 200 kV microscope (Zeiss, in column EELS filter, 200kV accelerating voltage) and spectra were collected in STEM mode (10 mrad illumination convergence semiangle and 15 mrad collection semiangle) and in TEM mode with 8 mrad convergence semiangle and 100 mrad collection semiangle without objective aperture at a 600000x magnification. The energy resolution was 0.75 eV with an energy dispersion of 0.06 eV/channel. The procedures developed and described elsewhere[45 – 49] were used to determine the complex dielectric function, energy band gap and volume change in ion-beam-irradiated HfO_2 samples from the valence part of EEL spectra. Plural scattering and the contribution of the zero-loss peak tail were deconvolved from the low-loss spectrum using the Fourier-log approach. Afterwards Kramers-Kronig analysis was performed using a low-loss single-scattering distribution to yield the energy dependence of the real and imaginary parts of the dielectric function using DigitalMicrograph GMS 2.31.

3. Results and Discussion

3.1. Chemical microanalysis and phase identification

Scheme of sample irradiation with Xe ions of primary energy (160 MeV) and reduced energy using thin Al films of varied thickness is shown in Figure 1a. shows a sample at Xe ion

irradiation with Al thin film used as ion energy reducer (a). FIB cross-section (Fig. 1b), HAADF STEM image (Fig. 1c) and the corresponding EDXS element map (Fig. 1d) with the element concentration profile (Fig. 1e) show the multilayered structure 1 μm SiO_2, 20 nm TiN bottom electrode, 10 nm La:HfO_2 dielectric and 20 nm TiN top electrode on the Si substrate. Quantitative EDXS was performed using a standardless routine using Cliff-Lorimer factors for thickness. Concentration of La was found to be 1.5 – 2.0 at % (Fig.1 e inset) what corresponds well with XPS data obtained by Chernikova et al [42] for the same samples. Despite some fluctuations in the concentration of elements at a distance of 5 nm (which often corresponds to the lateral size of crystals in the hafnium layer), the stoichiometric composition remains on average (Fig.1 e).

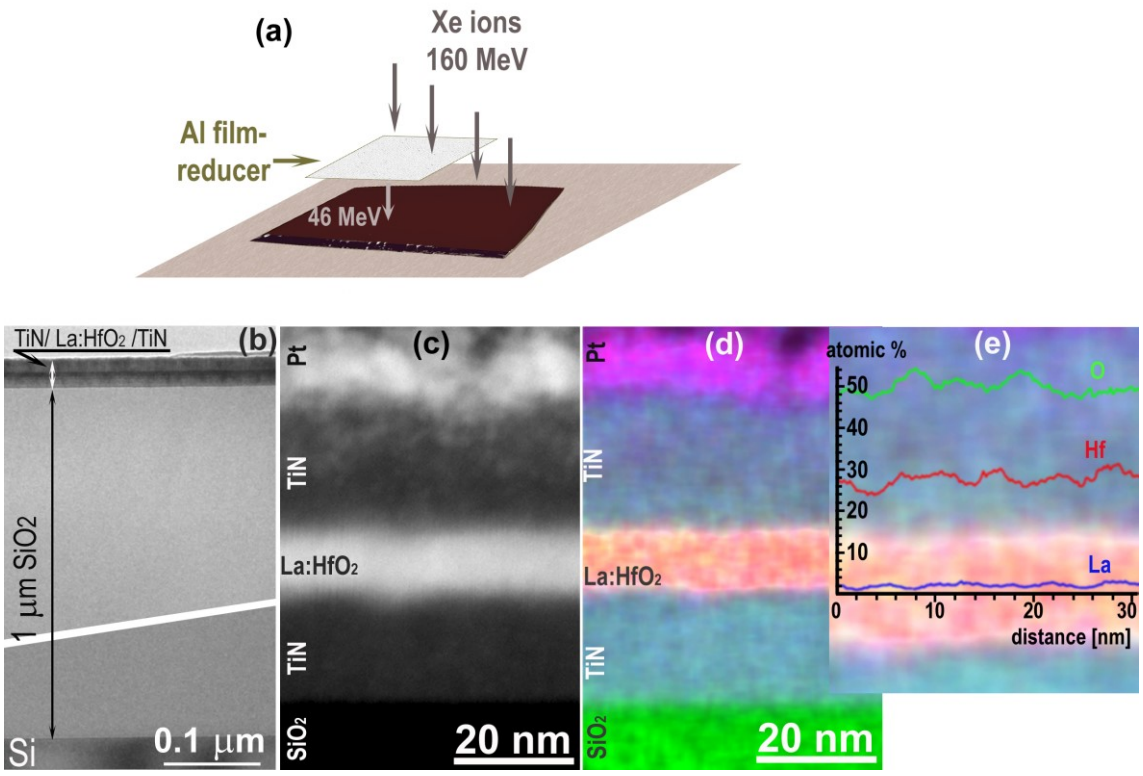

Figure 1. Scheme of irradiation of samples with Xe ions of different energy obtained using thin Al films of varied thickness as energy reducers (a), cross-section of the multi-layer sample (b), cross-section HAADF image (c) EDXS element map obtained in atomic % (d), the concentration profile of Hf, O and La in the La:HfO_2 layer on the EDXS element map (e).

The identification of phases present in the La:HfO_2 layer was performed on cross-sections by selected area diffraction (SAED). Polycrystal (ring) diffraction patterns were compared with JEMS[45] simulations for all known HfO_2 structures. Assuming that the doped and undoped HfO_2 are isomorphs, irradiated La:HfO2 with 160 MeV Xe ions exhibits (Fig. 2a) the tetragonal HfO_2 structure *P4₂/nmc* (7146-ICSD) while the nanocrystals in the pristine specimen have (Fig. 2b) the orthorhombic HfO_2 structure *Pbcm* (53034-ICSD), see Table S1 in Suppl. Materials. Samples irradiated with Xe ions of intermediated (24, 46 and 72 MeV) energy contain a mixture of these orthorhombic and tetragonal phases. The TiN (top and bottom electrodes) and Pt (deposited layer for FIB sample preparation) diffraction rings served as a calibration standard for phase analysis.

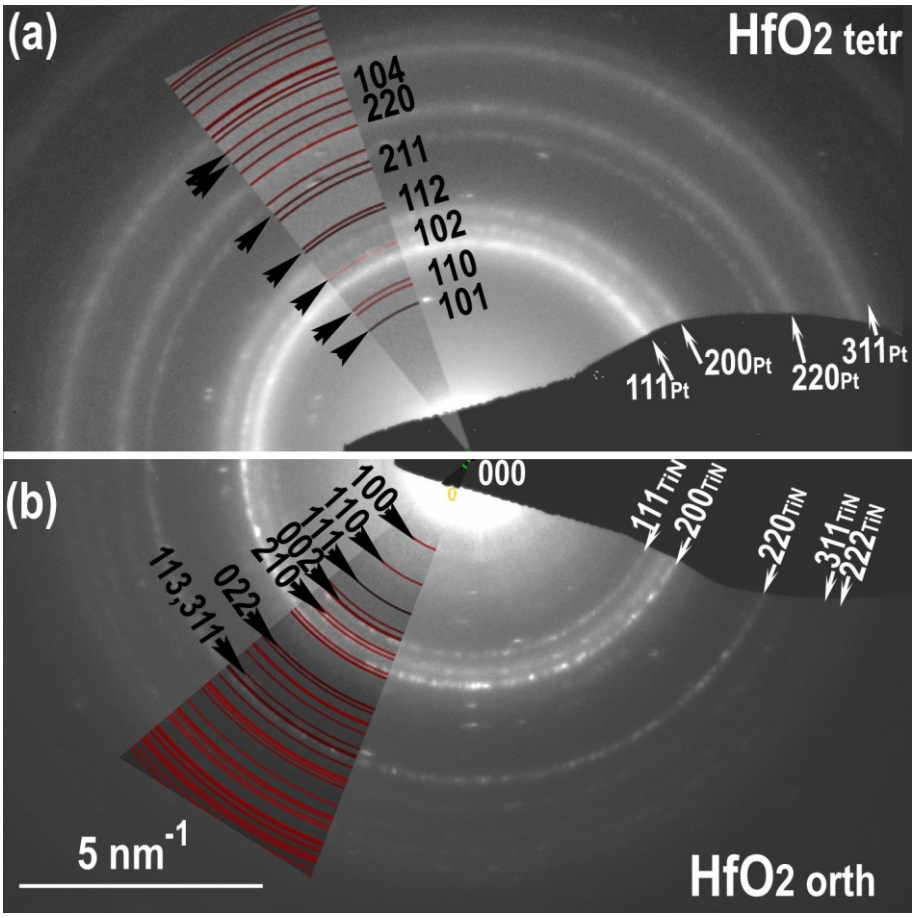

Figure 2. SAED of *P4₂/nmc* tetragonal HfO_2 phase in the sample irradiated with160 MeV Xe ions (a), SAED of *Pbcm* orthorhombic HfO_2 phase in the reference sample (b).
JEMS simulated rings are superimposed on the experimental diffraction patterns, the reflections of HfO_2 phases as well TiN and Pt reflections are pointed by arrows.

In addition to polycrystal ring SAED patterns, phase identification was performed on some 200 individual nanocrystals using HRTEM Fast Fourier Transform (FFT) diffractograms analysis and HRTEM multislice image simulation.

First, FFTs were obtained from HfO_2 crystal images and analyzed to derive the possible phases according to symmetry. However, one should be aware that the symmetry of the FFT of a 2-D phase image of the 3-D crystal structure may be different from that of the diffraction pattern. In addition, the resolution on the FFT is much lower than that of the diffraction pattern and reduces the accuracy of interplanar spacing measurement to some 5% or even worse. In counterpart, it brings the angle between non-coplanar atom planes that is lost in ring patterns and even with about 3% accuracy. Since the crystal parameters for different HfO_2 structures bring very similar diffraction patterns to each other, one cannot rely solely on FFTs. For instance, HfO_2 orthorhombic structures as well as monoclinic and tetragonal ones can match FFT diffractograms if the estimated measurement accuracy is only 5% and 3% for spacings and angles respectively. Second, identification ambiguities can only be resolved by comparing the atom pattern and contrasts of experimental HRTEM images with their counterparts on simulations for each phase accepted in the FFT approach. This part of the identification requires a tedious work as neither the nanocrystal thickness nor its misalignment with respect to the zone axis orientation suggested by the FFT diffractogram are known that leads to a long trial and error approach even if the optical parameters of the microscope are *a priori* known. Such a thorough analysis including image contrast matching between experimental HRTEM micrographs and image simulation has led to identify the true structure of La doped hafnia that differs from that found by Perevalov *et al*[50] in a TEM study without HRTEM simulation.

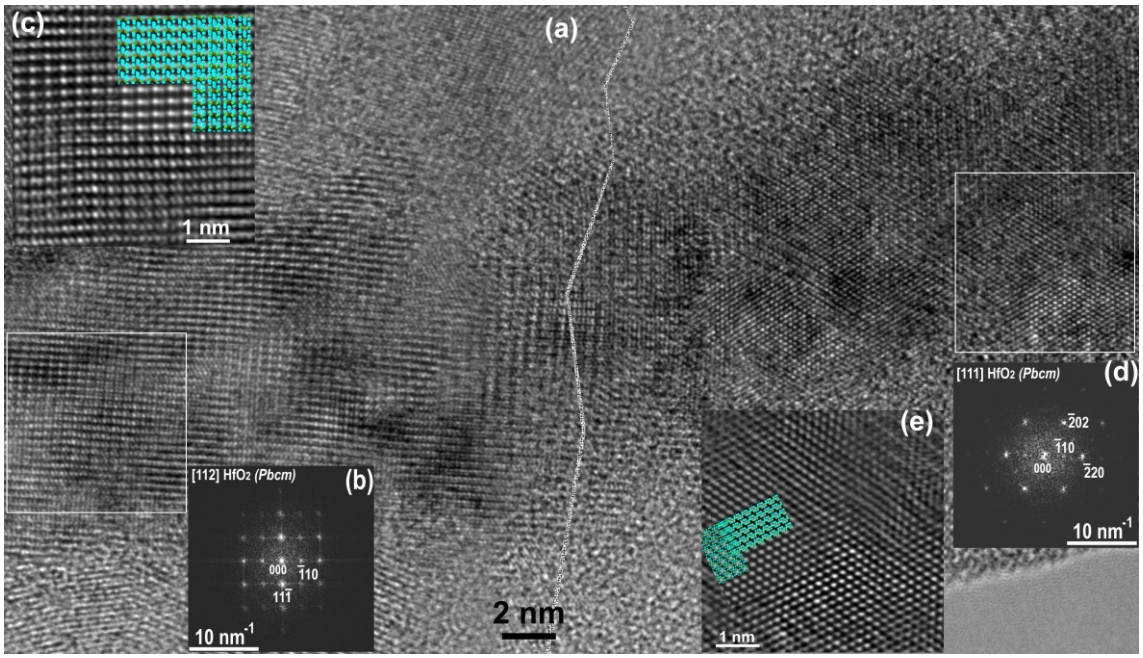

Figure 3. Cross-section HRTEM image from a pristine (non-irradiated) La:HfO_2 layer (a), FFTs interpreted as the diffractogram of a single crystal (b, d) and the atom plane lattice compared with simulated images using the multislice method (c, d) with superimposed Hf and O atoms were obtained using the orthorhombic *Pbcm* HfO_2 structure oriented along [112] (b, c) and [111] (d, e) directions.

Figure 3a shows the montage of two nearly adjacent HRTEM images obtained from the pristine HfO_2 layer. Nanocrystals are mainly equiaxed with random orientation and their overlap blurs the atom lattices on a large part of the layer image where a crystal occupies most or the whole sample thickness with a suitable orientation. The boundary between two images is shown with broken line. Two FFTs taken from the selected (white squares) 6.6 nm x 6.6 nm nanocrystals (Fig.3b and d) showed that they can have orthorhombic *Pbcm* structure and are oriented along the [112] and [111] directions. HRTEM simulated images with superimposed Hf and O atoms as well as the atomic structural models (inserts in Fig.3 c and e) corresponding to [112] and [111] *Pbcm* phase are in the good agreement with the experimental (filtered) HRTEM images. The enlarged

images with details of the microscope optics and image simulation conditions are present in Fig. S1 and S2 in the Supplementary Materials.

A similar approach for HRTEM images and FFT diffractograms interpretation led to show that the structure of nanocrystals in the La:HfO_2 layer is

- tetragonal $P4_2/nmc$ structure after irradiation with 160 MeV Xe ions (Fig. 4 and details on Fig S3 in Supplementary Materials);
- orthorhombic *Pbcm* structure after irradiation with 24 MeV Xe ions (Fig S4 in Supplementary Materials) like in pristine sample, although some FFT diffractograms have a convincing fit with the higher symmetrical *Pbca* orthorhombic structure;
- both *Pbcm* orthorhombic and tetragonal $P4_2/nmc$ phases after 46 MeV Xe irradiation (Figs. 5 and 6).

The hafnia layer irradiated with 46 MeV Xe ions contains the mixture of nanocrystals with orthorhombic *Pbcm* and tetragonal $P4_2/nmc$ structures. The TEM cross-section and the SAED pattern obtained from it are present in Fig. 5 a, b. The best match between experimental spotty rings and the simulated ones was achieved for the mixture of two HfO_2 phases – orthorhombic *Pbcm* and tetragonal $P4_2/nmc$. In opposite to the SAED patterns from the pristine sample two closest to the SAED center 100 and 110 diffraction rings from the orthorhombic phase were not observed probably because of texture formed after irradiation. Since the diffraction pattern contains spotty rings and not solid (unbroken) rings, it is impossible to conclude that the hafnia layer is textured from the SAED pattern. Therefore, HRTEM FFT diffractograms from single nanocrystals in the cross-section (Fig.5 a) were obtained and analyzed. According to the sequence of 13 FFTs obtained from 6.5 nm x 6.5 nm regions (Fig. 5c), single crystals can occupy some part or the entire layer thickness, while crystals with the tetragonal structure are oriented along the [111], and crystals with the orthorhombic structure along the [101] directions (indexes are shown in Fig. 6).

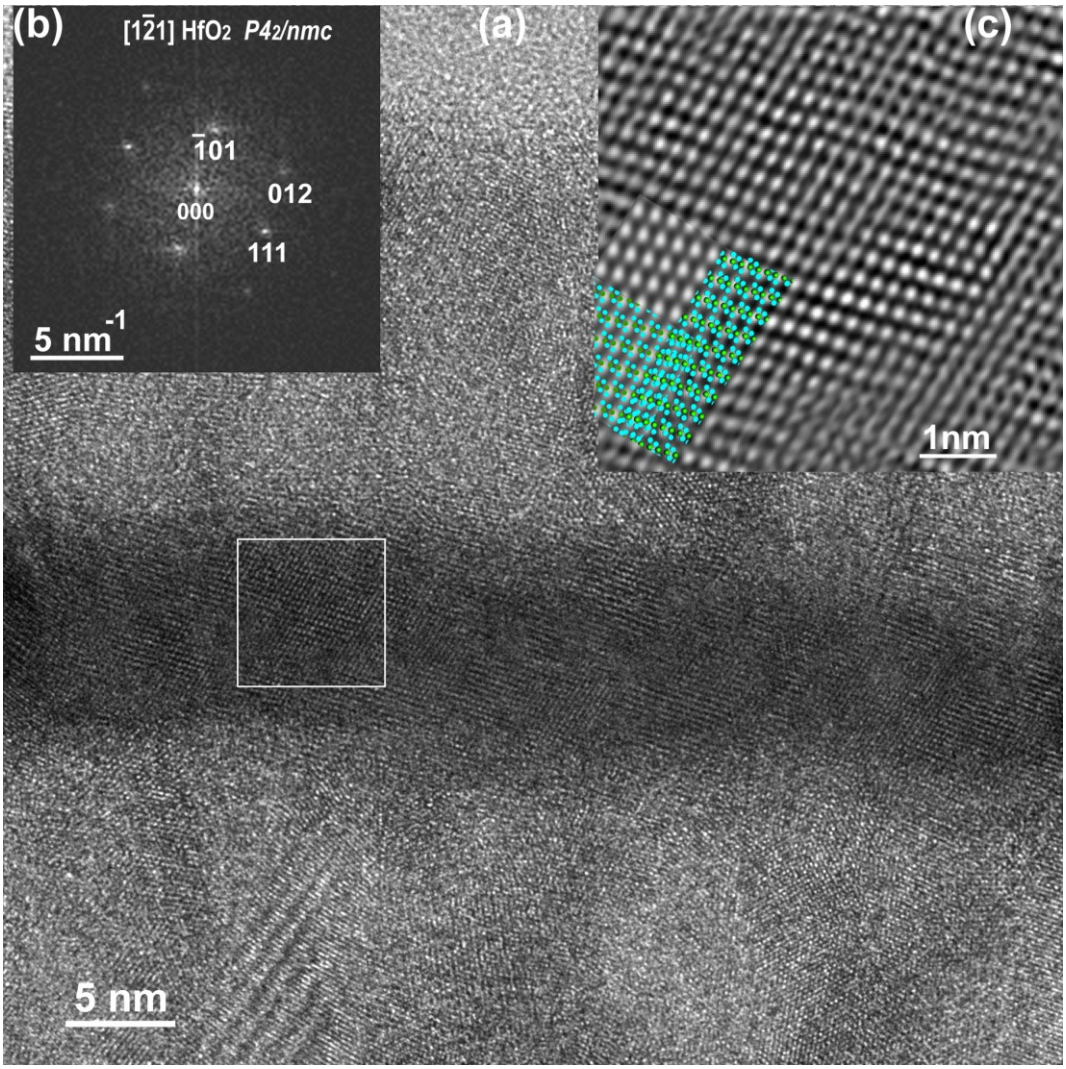

Figure 4. Cross-section HRTEM image from a 160 MeV Xe ion irradiated La:HfO_2 layer (a) FFT interpreted as the diffractogram of a single crystal (b), enlarged HRTEM image and the atom plane lattice compared with the simulated image and superimposed Hf and O atoms (c) from the selected 6.6 nm x 6.6 nm area obtained from the HfO_2 crystal with tetragonal *$P4_2/nmc$* structure along the [1-21] direction.

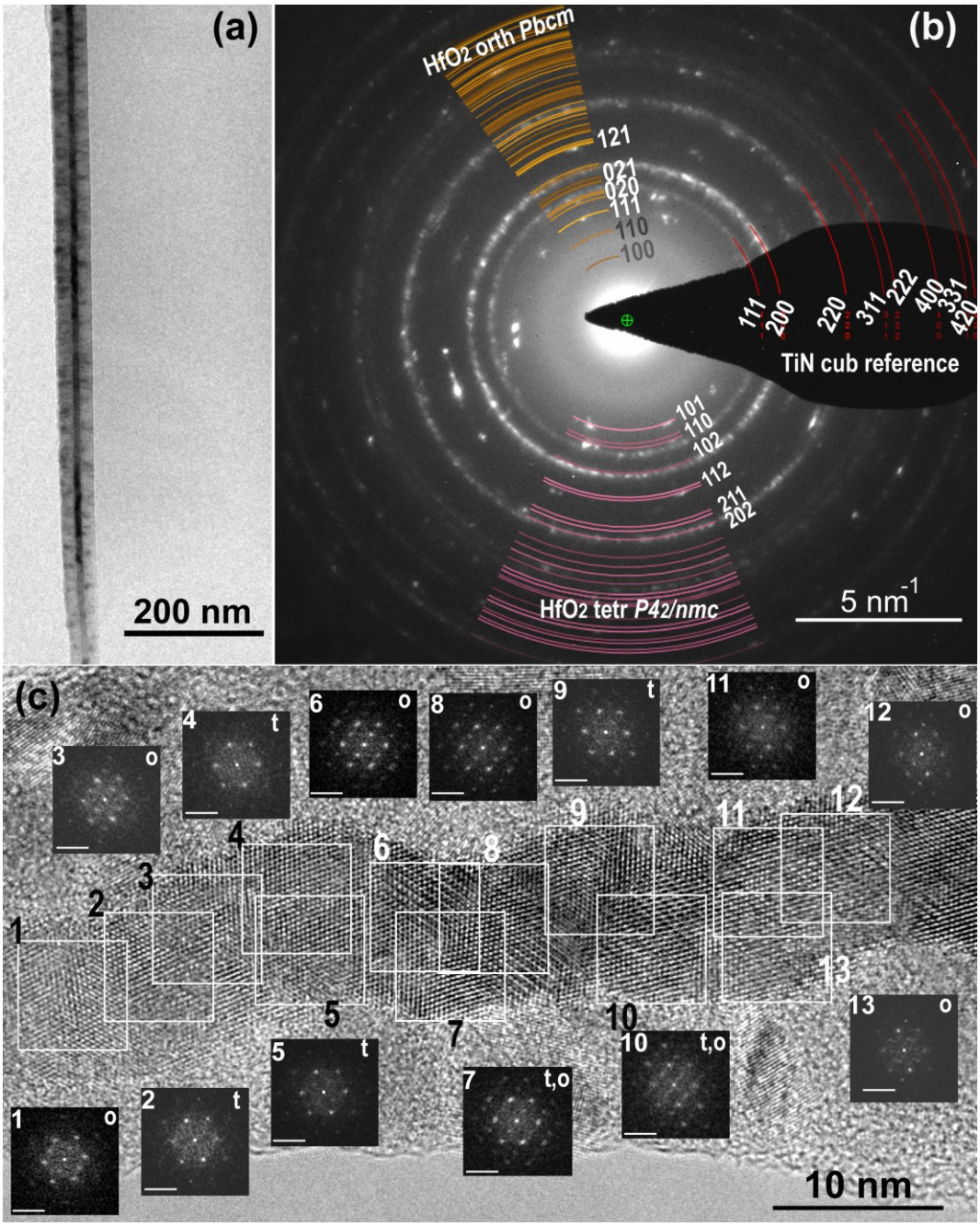

Figure 5. TEM cross-section of La:HfO_2 layer irradiated with 46 MeV Xe ions (a); SAED taken from the TEM cross section and insets with JEMS simulated rings from HfO_2 orth *Pbcm*, HfO_2 tetr *P4₂/nmc* and TiN as reference superimposed on the SAED rings with the reflections of HfO_2 phases TiN (b); distribution of HfO_2 nanocrystals with orthorhombic *Pbcm* and tetragonal *P4₂/nmc* structures along the cross-section and FFTs were obtained from each 6.5 nm x 6.5 nm white square region, labeled 1 – 13 with "o" and "t" corresponding to orthorhombic and tetragonal phases (c).

Figure 6a shows the HRTEM image from nanocrystals after 46 MeV Xe ion irradiation. The FFTs (Fig.6 b and c) identified, respectively, 3.3 nm x 3.3 nm areas selected by white squares as La:HfO_2 [101] orthorhombic *Pbcm* and tetragonal $P4_2/ncm$ [111]. This is confirmed by the HRTEM simulations in inserts "tetr" and "orth". The FFT from the whole figure area (Fig. 6d) shows that orthorhombic and tetragonal nanocrystals take each a single orientation that corresponds to an epitaxial relationship [111](1-10) HfO_2 tetr // [101](010) HfO_2 orth. HRTEM and FFTs show that the HfO_2 crystallographic orientations are not random in the part of the layer taken for TEM, but have some preferred orientation along the orthorhombic {-111} and tetragonal {-101} directions. The texture is retained for other 77 and 160 MeV Xe ion irradiated samples.

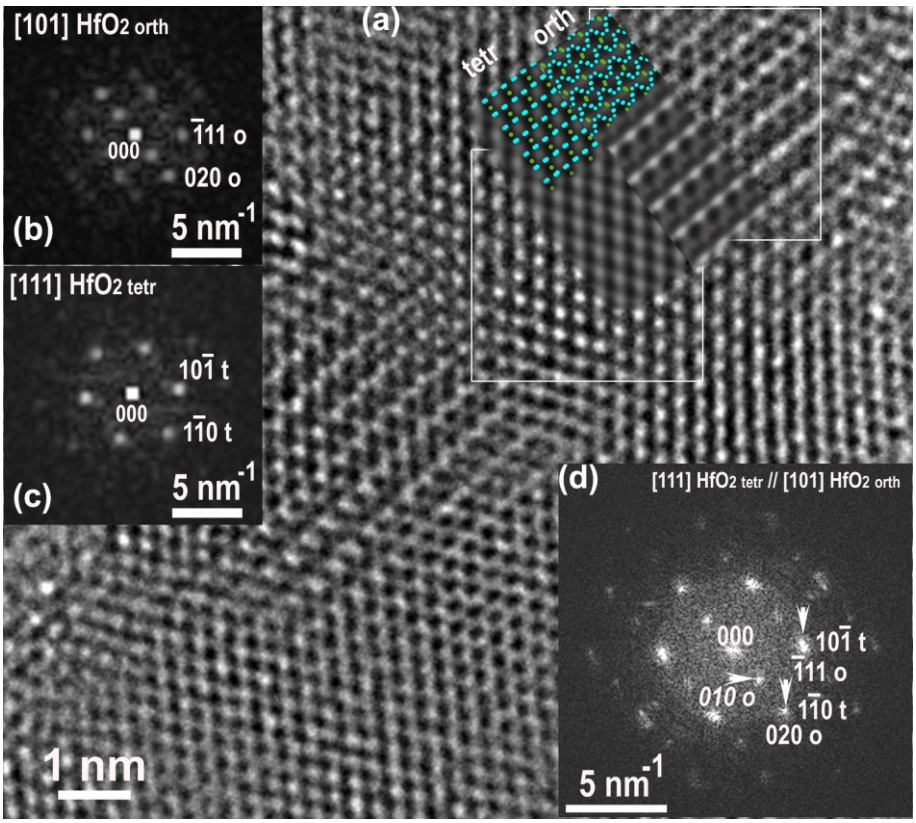

Figure 6. HRTEM image of HfO_2 layer obtained from the 46 MeV Xe irradiated sample (a), , FFTs obtained from single HfO_2 nanocrystal images with orthorhombic *Pbcm* and tetragonal $P4_2/nmc$ structure along the [101] and [111] directions (b and c); FFT obtained from the whole HRTEM images with crystallographic relationships[111](1-10) HfO_2tetr // [101](010) HfO_2orth. **Insets** on the HRTEM image: JEMS HRTEM simulations with superimposed Hf and O atom positions for the orthorhombic and tetragonal structures along the $[101]_{orth}$ and $[111]_{tetr}$ directions for the defocus value within 40-45 nm and crystal thickness of 90 nm, HV 200 kV, *Cs*1.2mm, *Cc* 1.1 mm.

A similar mixture of HfO_2 nanocrystals with tetragonal and orthorhombic structure was observed also in hafnia layer irradiated with 77 MeV Xe ions.

Amorphization was never observed in La:HfO_2 nor in TiN top and bottom electrodes.

3.2. Evaluation of the temperature field in swift Xe ion tracks in HfO_2 and discussion of the mechanism of phase transformation

Due to large amount of energy transferred into electron subsystem, the structural effects of SHI irradiation are associated with local heating and subsequent rapid quenching in the region surrounding ion trajectory. The TSPIKE02 code, built on the basis of inelastic thermal spike (i-TS) model[51] was used to evaluate the temperature in the vicinity of Xe ion trajectories. As Weber et al.[52] noted in their work, this semi-empirical model is a useful tool for analyzing experimental results, but one should keep in mind that the model is built on several approximations. In particular it does not take into account phenomena such as shock waves and radiative processes, nor effects of superheating. Here, we attempt to phenomenologically explain the SHI irradiation induced structural changes as the result of recrystallization from the melt into a new phase or a direct crystal-to-crystal phase transition in hafnia nanocrystals 5-15 nm in size in lateral direction and up to 10 nm in height.

Table 2. Thermodynamic parameters for HfO_2.

Thermal conductivity (W/m·K)	1.1
Specific heat capacity (J/kg·K) at 300 K	≈ 120
Melting temperature (K)	3050 – 3173
Heat of fusion (J/g)	120-250
Boiling temperature (K)	≈ 5000

The i-TS model uses two coupled equations governing the energy diffusion into the electron and lattice subsystems and the energy transfer between two systems with the electron mean free path λ as the only open parameter. In our calculations, the open i-TS parameter λ was equal 4.3 nm,

a typical value for crystalline inorganic insulators[51]. Other parameters[53, 54], namely melting temperature, specific heat capacity, thermal conductivity are summarized in Table 2.

The results of the temperature **T** evolution versus time **t** in HfO_2 close to the Xe ion trajectory are given in Fig. 7.

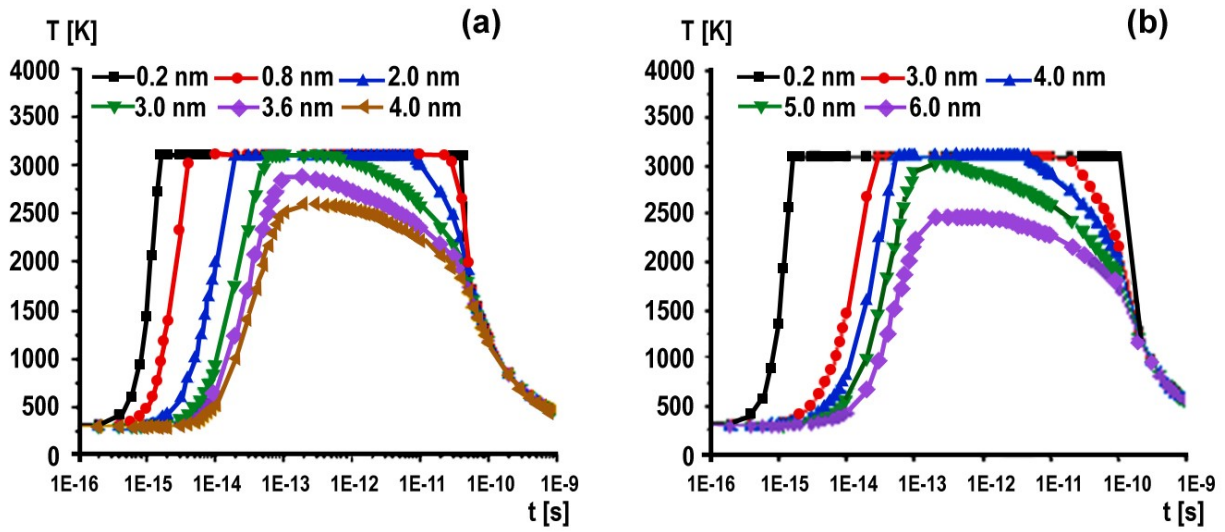

Figure 7. Temperature evolution at different radial distances from the Xe ion axis with the energy 46 MeV (0.35 MeV/u) and S_e =16.4 keV/nm (a) and 160 MeV (1.22 MeV/u) and S_e =29.5 keV/nm (b).

As you can see, the temperature in the vicinity Xe ion trajectory reaches a melting temperature of 3100 K at radii ≈3 nm for energy loss of 16.4 keV/nm (Fig.7 a) and ≈5 nm for the largest energy deposition of 29.5 keV/nm (Fig.7 b). At the same time, the plateau regions in Fig. 7 demonstrate that energy transferred to lattice atoms (heat of fusion) is less than needed to change the material from solid to liquid state (T_{boil} 5000K) and this may explain the absence of amorphous phase in HfO_2 at current irradiation conditions. The presence of both orthorhombic and tetragonal crystallites observed in hafnia samples irradiated with 46 MeV Xe ions implies that the threshold electron stopping power of corresponding phase transition is about 16 keV/nm.

Therefore, the structural change from the orthorhombic to tetragonal phase can be attributed to crystalline - crystalline phase transition. However, it should be noted that thermodynamics

parameters of HfO_2 were taken from equilibrium measurements and their values differ from one author to another. Moreover, the electron mean free path values are not precisely known for hafnia. Therefore, more experimental evidences are still required to describe and understand the mechanism of structure changes under irradiation with different energy.

3.3. Determination of bandgap and dielectric functions with VEELS

Valence EELS (VEELS) was used to investigate the properties - the bandgap and dielectric function - of the pristine, 46 MeV and 160 MeV Xe ion irradiated La:HfO_2 thin layers. VEELS spectra were acquired in TEM and STEM modes in the middle of the La:HfO_2 layer between the two TiN electrodes with an exposure time of 1 s and an energy dispersion of 0.06 eV per channel. The quantification was performed only for the spectra in which the intensity of the first plasmon peaks was less than one tenth of the zero loss intensity, which suggests that the cross-sectioned specimens are thin enough. The single scattering distribution (SSD) or the energy-loss function (ELF) by plural scattering deconvolution from the original spectra using DigitalMicrograph routine was obtained. To minimize the thickness effect on the band gap value care was taken to compare the data obtained from the areas of different specimens with the similar thicknesses. Matching HRTEM micrographs and their image simulation showed that their thickness was in the range 40 to 90 nm. This sample thickness was favorable since it allowed to escape the presence of surface plasmons which would make interpretation more complex.

Plasmons are the most important features measurable in low loss spectrum region by VEELS. The behavior of valence electrons[46, 55] in insulators is described within the framework of the “free-electron gas” or “jellium” model, and a collective oscillation of the electron density occurs at a characteristic angular frequency ω_p (plasmon frequency in radians per second) which is given by $\omega_p = [ne^2/(\varepsilon_0 m)]^{1/2}$, where n – electron density, e – electron charge, ε_0 – vacuum permittivity, and

m – particle mass. Plasmon energy is $E_p = \hbar\omega_p$ and can be expressed as $E_p = \hbar[(z\rho/uM)e^2/(\varepsilon_0 m_0)]^{1/2}$, where z - is the number of free (valence) electrons per molecule, u is $1/N_A$, M is molecular weight, ρ is the density in g/cm^3, and $m = m_0$ (electron rest mass). Thus the *free-electron* plasmon energy is evaluated as $E_p = (28.82\ \text{eV})(z\rho/M)^{1/2}$ with M, z and ρ for a given compound. Therefore, for the compound with the same chemical composition but a different structure, the larger E_p implies a higher valence-electron density, resulting from shorter interatomic distances and/or a larger number of valence electrons per molecule, both of which leading to stronger interatomic bonding.

However, the energy position of the plasmon losses can be influenced considerably by several different factors, such as the potential of the ion cores and Coulomb interaction between the valence electrons[55]. The plasmon energy E_p of HfO_2 thin layer correlates with its structure and morphology [36]. A significant red shift of the bulk plasmon peaks was observed with increasing structural disorder in SiC during irradiation[56]. To estimate a volume expansion of the amorphous part of 6H-SiC after irradiation, Jiang et al.[57] proposed an expression that relates the plasmon loss energy shift and the relative volume change.

In our work, after irradiation, the plasmon energy loss peak, E_p, experiences a shift to higher energy from 14.9 in the pristine La:HfO_2 to 15.4 eV in the 46-MeV and 15.9 eV in 160-MeV irradiated sample (Fig. 8). Thus, in comparison with the pristine hafnia, the bulk plasmon peak of the tetragonal HfO_2 is blue-shifted by 1.0 eV, which should indicate that following the irradiation the atomic density increased in accordance with the conclusions in the papers [56, 57]. However, the material density of the tetragonal HfO_2 phase is by 4.5% less than the density of the orthorhombic HfO_2 phase (Table 1 in Suppl. Materials). In tetragonal HfO_2 structure the coordinating number of Hf is 8 while in in the orthorhombic phase is 7. Thus, this result suggests that an element with a higher coordination number has more possible electron density regions around it, and an element with a lower coordination number has fewer possible electron density regions around it. Therefore, we observed the blue-shift plasmon energy in tetragonal HfO_2.

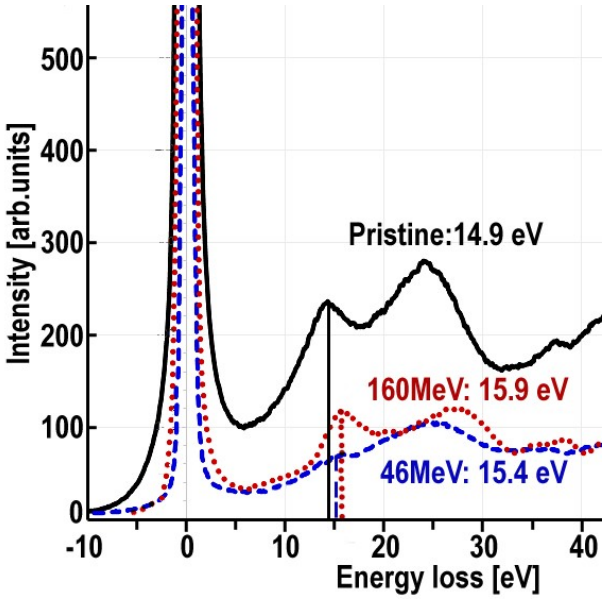

Figure 8. Low-loss EELS spectra showing that the magnitude of the blue shift of the bulk plasmon peak increases when the structure transformation occurs from the orthorhombic to tetragonal phase in hafnia layer at the Xe ion energy irradiation.

In addition to the plasmon position shift, a large intensity difference was observed on the plasmon peaks around ~15 eV for the 46 MeV irradiated relatively to 160 MeV and pristine samples in VEELS spectra (Fig. 8) and the energy loss functions (Fig. 9). The broaden and damped plasmon peak is characteristic of the 46 MeV Xe ion irradiation layer, both in very thin and thicker areas of the TEM sample (Fig.5 a).

Among several factors affecting the line shape of plasmon peaks, there may be multiple scattering in thick samples. In the present work, to extract the true plasmon line shape from the experimental spectra, multiple scattering was mathematically removed using Fourier-log deconvolution routines in Digital Micrograph. Energy resolution could be another concern but it was kept constant for all samples and low enough (0.7 eV) to have a negligible effect.

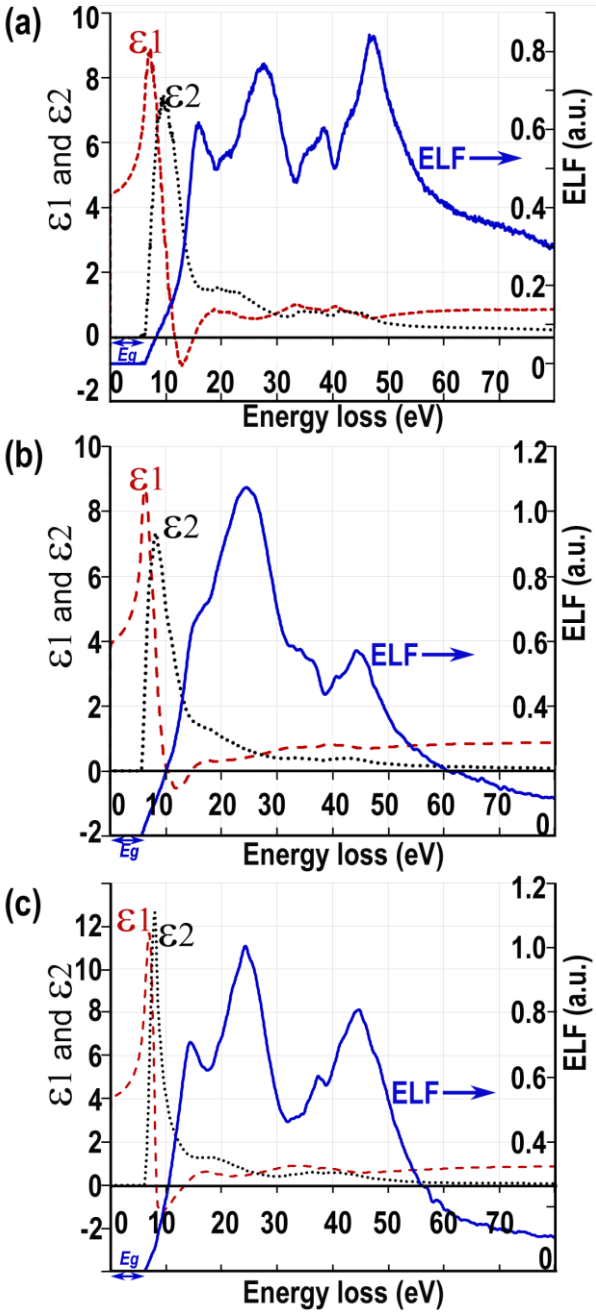

Figure 9. Electron-energy loss functions (ELF), real and imaginary dielectric functions ε1 and ε2 derived from low-loss EEL spectra of the La:HfO_2 layers irradiated with 160 MeV Xe ions (a), 46 MeV Xe ions (b) and pristine sample (c). Peak at ~15 eV corresponds to a bulk plasmon of HfO_2. The energy *Eg* of the intensity thresholds in the HfO_2 film from pristine and irradiated (160 MeV Xe ions, and 46Mev) layers, which is a measure of the band gap, are shown.

Eventually the profile and intensity of plasmon peaks depends on the material and sample properties. The changes in spectrum shapes in the energy interval 14 – 20 eV for the hafnia layer were attributed to different structure and morphology[36] , to the content of oxygen[58, 59]: low-oxygen ALD hafnia layer had EELS spectra with absolutely damped peak at 15 eV, while high-oxygen hafnia powder with submicron sized grains demonstrated well-developed plasmon peak at 15 eV in spite that the EDXS did not show lower oxygen concentrations in ALD HfO_2 layers [58].

Guedj et al.[60] showed by *ab initio* calculations using the time-dependent density-functional theory (DFT) that plasmon peaks are modified as a function of the crystallographic orientation of monoclinic HfO_2 crystals or precisely they claimed that the direction of momentum transfer affects peak amplitude and the shoulder of the averaged spectrum becomes a well-defined peak in certain directions and, in particular, in [001] oriented crystals, while it is disappearing in [11-1] oriented crystals.

Summarizing all the arguments, it is most likely that in the poly(nano)crystalline structure, the profile of the plasmon peak can be damped depending on the number of crystals with the given orientations. In addition, our TRIM calculations did not show an increase in oxygen vacancies in 46MeV irradiated hafnia layer as compared to the sample irradiated with 160 MeV Xe ions.

The bandgap averaged from 10 EELS spectra for each sample (Fig. 9) underwent insignificant changes within the experimental confidence interval (standard deviation) from 6.1±0.2 eV for pristine La:HfO_2 layer to 6.2±0.3 for 46 MeV and 6.3±0.2 eV for 160 MeV Xe ion irradiated samples.

Thus, this observation confirmed that bandgap does not strongly depend on HfO_2 structure as well possible effects a species diffusing at interfaces or density of vacancies/interstitials after irradiation. Cheynet et al. [36] measured 5.9±0.5 eV in pure orthorhombic HfO_2. This difference is of the same order of magnitude as the confidence interval, therefore too small to ascertain that doping

HfO_2 with La increases the bandgap. It is nevertheless compatible with the trend reported by Murat and Medvedeva[61] of a bandgap increase by incorporation of lighter metals in multicomponent oxides.

The complex dielectric function (the real part ε1 and imaginary part ε2) was obtained by use of the Kramers–Kronig approach[47]. Figure 9 shows the dielectric functions ε1 and ε2 calculated with Digital Micrograph for the 160 MeV (Fig.9 a), 46 MeV Xe (Fig.9 b) ion irradiated layer and the pristine layer (Fig.9 c). The values of the dielectric constants ε1 is in the range 4.2- 4.6 in points of intersection of the y-axis of the curve (at the zero energy) are in agreement with the values obtained for the monoclinic HfO_2 by Park and Yang[62] and are approximately equal to the square of the refractive index $\boldsymbol{n}_{HfO2}$ ≈2.10-2.16. In this part of our study we can confirm the results of Singh et al.[40] that the dielectric functions did not change significantly with ion irradiation in the given range of ion energy.

4. Conclusions

The crystal structure, dielectric function and energy band gap of La:HfO_2 layer in 20nm TiN/10nm La:HfO_2/20nm TiN/1 μm SiO_2/Si stack have been investigated by TEM, HRTEM, electron diffraction, EDXS and EELS. Their changes between pristine and swift Xe ion irradiated (0.13 – 1.20 MeV/u) samples are reported.

No amorphization of La:HfO_2 was found under any irradiation conditions. Pristine La:HfO_2 thin films contained nanocrystals of 5 – 20 nm hafnia nanocrystals with orthorhombic structure (sp. gr. *Pbcm*). Their irradiation with the most energetic 160 MeV Xe ions introduces a phase transformation to hafnia nanocrystals with $P4_2/nmc$ tetragonal structure. At intermediate ion energies 46 and 77 MeV a mixture of orthorhombic and tetragonal phases is formed. At the lowest energy, 24 MeV, a mixure of nanocrystals with orthorhombic structure but different space groups *Pbcm* and *Pbca* were found showing that part of the sample kept the pristine structure and part of it

was transformed. The textured hafnia layers were formed as a result of irradiation with 46, 77 and 160 MeV Xe ions.

The structural changes and crystal orintations in hafnia layer affect the shape and energy position of low-loss plasmon peaks in VEELS spectra. The band gap for orthorhombic (6.1 eV), mixed orthorhombic-tetragonal (6.2 eV), and tetragonal (6.3 eV) HfO_2 phases were measured by VEELS. Measurements showed that the dielectric functions (real and imaginary) and the band gap changed insignificantly as a result of structural rearrangement after ion irradiation.

SUPPLEMENTARY MATERIAL.

The supplementary material contains

- a table of known HfO_2 lattice parameters, space groups and conditions of observations from literature,

- more detailed examples of phase identification with FFT diffractogram indexing and HRTEM image simulation for each irradiation energy.

AUTHORS'S CONTRIBUTION

All authors contributed equally to this work.

DECLARATION of COMPETING INTEREST

The authors declare that there is no conflict of interests regarding the publication of this article.

ACKNOWLEDGEMENTS

This work was carried out using the equipment of the Shared Research Centers of A.V. Shubnikov Institute of Crystallography, FSRC "Crystallography and Photonics" and Prokhorov General Physics Institute RAS and supported by the Ministry of Science and Higher Education of the Russian Federation.

The data that supports the findings of this study are available within the article [and its supplementary material].

The authors gratefully thank Prof. A. M. Markeev and his team from the Moscow Institute of Physics and Technology for producing the TiN/HfO_2/TiN/SiO_2 /Si stacks by atomic layer deposition.

References

1. O. Ohtaka, H. Fukui, T. Kunisada, T. Fujisawa, K. Funakoshi, W. Utsumi, T.Irifune, K. Kuroda, and T. Kikegawa, J. Am. Ceram. Soc., **84**, 1369 (2001).

2. R. Suyama, H. Horiuchi, and S. Kume, J. Ceram. Soc. Japan. 95, 567 (1987).

3. D.M. Adams, S. Leonard, D. R. Russell, and R. J. Cernik, J. Phys. Chem. Solids **52**, 1181 (1991).

4. D. Fischer and A. Kersch, The effect of dopants on the dielectric constant of HfO_2 and ZrO_2 from first principles, Appl. Phys. Lett. **92**, 012908 (2008)

5. J. Wang, H.P. Li, and R. Stevens, J. Mater. Sci. **27**, 5397 (1992).

6. S. Pathak, P. Das, M. Sahu, K. L. Pandey, G. Mandal, and G. R. Patkare. High Pressure Res. (2020), https://doi.org/10.1080/08957959.2020.1765338.

7. J. Robertson, Eur. Phys. J. Appl. Phys., **28**, 265 (2004).

8. A. J. Vuuren, V.A. Skuratov, V.V. Uglov, J.H. Neethling, and S.V. Zlotski, J. Nucl. Mater. **442,** 507 (2013).

9. Y. Zhang, D. S. Aidhy, T. Varga, S. Moll, P. D. Edmondson, F. Namavar, K. Jin, C. N. Ostrouchov, and W. J. Weber, Phys. Chem. Chem. Phys. **16,** 8051 (2014).

10. W. F. Cureton, R. I. Palomares, J. Walters, C. L. Tracy, C.-H. Chen, R. C. Ewing, G. Baldinozzi, J. Lian, C. Trautmann, and M. Lang, Acta Mat. **160**, 47 (2018).

11. K. E. Sickafus, Hj. Matzke, Th. Hartmann, K. Yasuda, J.A. Valdez, P. Chodak, M. Nastasi, and R.A. Verrall, J. Nucl. Mat. **274**, 66 (1999).

12. E. I. Suvorova, P. N. Degtyarenko, I. A. Karateev, A. V. Ovcharov, A. L. Vasiliev, V. A. Skuratov, P.A. Buffat, J. Appl. Phys. **126**, 145106 (2019)

13. A. Benyagoub, Nucl. Instrum. Meth. **B 218**, 451 (2004).

14. A. Benyagoub, Phys. Rev. **B 72**, 094114 (2005).

15. Z. Li, J. Liu, P. Zhai, T. Liu, J. Bi, Z. Zhang, S. Zhang, P. Hu, L. Xu, J. Zeng, and Y. Sun. IEEE Electron Device Letters **40**, 1634 (2019).

16. X. Zhao and D. Vanderbilt. Phys. Rev. **B 65**, 233106 (2002)

17. Q. Zeng, A.R. Oganov, A.O. Lyakhov, C. Xie, X. Zhang, J. Zhang, Q. Zhu, B. Wei, I. Grigorenko, L. Zhang, and L. Cheng, Acta Cryst. **C 70**, 76 (2014).

18. E. Bersch, S. Rangan, and R.A.Bartynski, Phys. Rev. **B 78**, 085114 (2008).

19. M. Vargas, N.R. Murphy, and C.V. Ramana, Opt. Mater. **37**, 621 (2014), pp.–628

20. M.-G. Blanchin, B. Canut, Y. Lambert, V. S. Teodorescu, A. Barău, and M. Zaharescu, J. Sol-Gel. Sci. Technol. **47**, 165 (2008).

21. F. L. Martínez, M. Toledano-Luque, J. J. Gandía, J. Cárabe, W. Bohne, J. Röhrich, E. Strub, and I. Mártil. J. Phys. D Appl. Phys. **40**, 5256 (2007).

22. J. E. Jaffe, R. A. Bachorz, and M. Gutowski, Phys. Rev. **B 72**, 144107 (2005)

23. K. Tomida, K. Kita, A. Toriumi, Appl. Phys. Lett. **89**, 142902 (2006).

24. F. M. Li, B.C. Bayer, S. Hofmann, J. D. Dutson, S. J. Wakeham, M. J. Thwaites, W. I. Milne, A. J. Flewitt, Appl. Phys. Lett. **98**, 252903 (2011)

25. M. T. Thomas, J. Electrochem. Sot. 117 (1970), pp. 396- 403

26. M. Balog, M. Schieber, M. Michman, S. Patai. Thin Solid Films 41 (1977), pp. 247-259

27. T. S. Böscke, S. Govindarajan, P. D. Kirsch, P. Y. Hung, C. Krug, B. H. Lee, J. Heitmann, U. Schröder, G. Pant, B. E. Gnade, and W. H. Krautschneider, Appl. Phys. Lett. **91**, 072902 (2007).

28. C. Adelmann, V. Sriramkumar, S. Van Elshocht, P. Lehnen, T. Conard, and S. De Gendt, J. Appl. Phys. **91**, 162902 (2007).

29. D. Fischer and A. Kersch, Appl. Phys. Lett. **92**, 012908 (2008)

30. Q. Tao, G. Jursich, P.Majumder, M. Singh, W. Walkosz, P.Gu, R. Klie, and C. Takoudis, Electrochem. Solid St. **12**, G50 (2009).

31. S. Govindarajan, T. S. Böscke, P. Sivasubramani, P. D. Kirsch, and B. H. Lee, Appl. Phys. Lett. **91**, 062906 (2007).

32. C. Dubourdieu, E. Rauwel, H. Roussel, F. Ducroquet, B. Holländer, M. Rossell, G. Van Tendeloo, S. Lhostis, S. Rushworth. J. Vac. Sci. Technol. **A 27**, 503 (2009).

33. Yu Zhang, Jun Xu, Da-Yu Zhou, Hang-Hang Wang, Wen-Qi Lu, and Chi-Kyu Choi, Chin. Phys. **B 27**, 048103 (2018).

34. S. Chen, Z. Liu, L. Feng, X. Che, and X. Zhao, Appl. Phys. Lett. **103**, 132902 (2013).

35. T. V. Perevalov, V. A. Gritsenko, S. B. Erenburg, A. M. Badalyan, H. Wong, and C. W. Kim, J. Appl. Phys.**101**, 053704 (2007).

36. M. C. Cheynet, S. Pokrant, F. D. Tichelaar, and J.-L.Rouvière, J. Appl.Phys. 101, 054101 (2007).

37. J. G. Bendoraitis and R. E. Salomon, J. Phys. Chem. **69**, 3666 (1965).

38. S. Migita, Y. Watanabe, H. Ota, H. Ito, Y. Kamimuta, T. Nabatame, and A. Toriumi, Design and Demonstration of Very High-k (k~50) HfO_2 for Ultra-Scaled Si CMOS. 2008 Symposium on VLSI Technology, Honolulu, HI, **152** (2008).

39. Y. Morita, S. Migita, W. Mizubayashi, M. Masahara, and H. Ota, Solid-State Electron. **84**, 58 (2013).

40. V. Singh, N. Shashank, D. Kumar, R. Nahar, Radiat. Eff. Defects in Solids **166,** 80 (2011).

41. K. Y. Ahn, L. Forbes, Atomic layer deposited lanthanum hafnium oxide dielectrics, Patent US 2006/01 281 68 A1 (2006).

42. A. G. Chernikova, D. S. Kuzmichev, D. V. Negrov, M. G. Kozodaev, S. N. Polyakov, A. M. Markeev, Appl. Phys.Lett. **108**, 242905 (2016)

43. J. F. Ziegler and J. P. Biersack, see http://www.srim.org/SRIM/SRIMLEGL.htm for "SRIM (The Stopping and Range of Ions in Matter (2013).

44. P. Stadelmann, see http://www.jems-swiss.ch/ for JEMS: Java Electron Microscopy Software (2019).

45. D.B. Williams, C. B. Carter, Transmission Electron Microscopy. A Textbook for Materials Science, Springer, Second Ed., New York, Chapters 38 and 39 (2009).

46. R.F. Egerton, Electron Energy-Loss Spectroscopy in the Electron Microscope, third ed., Springer, New York, 2011.

47. M. Stöger-Pollach, A. Laister, and P. Schattschneider, Ultramicroscopy **108**, 439 (2008).

48. P.L. Potapov, H.-J. Engelmann, E. Zschech, and M. Stöger-Pollach, Micron **40**, 262 (2009).

49. R. Sachan, O. H. Pakarinen, P. Liu, M. K. Patel, M. F. Chisholm, Y. Zhang, X. L. Wang, and W. J. Weber, J. Appl. Phys.117, 135902(2015)

50. T. V. Perevalov, A. K. Gutakovskii, V. N. Kruchinin, V. A. Gritsenko, and I. P. Prosvirin, Mater. Res. Express **6**, 036403 (2018).

51. M. Toulemonde, Ch. Dufour, A. Meftah, and E. Paumier, Nucl. Instr. Meth. **B 166-167**, 903 (2000).

52. W. J. Weber, D. M. Duffyc, L. Thoméd, and Y. Zhang, Curr. Opin. Solid State Mater. Sci. **19**, 1 (2015).

53. Qi-Jun Hong, S.V. Ushakov, D. Kapush, C. J. Benmore, R. J. K. Weber, A. van de Walle, and A. Navrotsky, Sci. Rep. **8**, 14962 (2018).

54. Thermodynamics of Certain Refractory Compounds, Ed. H.L. Schick, **1**, pp.1-266 – 1-282 (1966).

55. D. Pines, Rev. Modern Physics **28**, 184 (1956).

56. C.M. Wang, Y. Zhang, W.J. Weber, W. Jiang, and L.E. Thomas, J. Mater. Res., **18**, 772 (2003).

57. W. Jiang, C. M. Wang, W. J. Weber, M. H. Engelhard, and L. V. Saraf, J. Appl. Phys. **95**, 4687 (2004)

58. J.H. Jang, H.-S. Jung, J.H. Kim, S. Y. Lee, C.S. Hwang, and M. Kim, Appl. Phys. Lett. **109**, 023718 (2011).

59. Chao Li, Y.Yao, Xi Shen, Y. Wang, Junjie Li, C. Gu, R.Yu, Qi Liu, and M. Liu, Nano Research **8**, 3571–3579 (2015)

60. C. Guedj, L. Hung, A. Zobelli, P. Blaise, F. Sottile, and V. Olevano, Appl. Phys. Lett. **105**, 222904 (2014).

61. A. Murat and J. E. Medvedeva, Phys. Rev. B 85, 155101 (2012)

62. J. Park and M. Yang, Micron **40**, 365 (2009).

SUPPLEMENTARY MATERIAL to

"Structure evolution, bandgap and dielectric function in La-doped hafnium oxide thin layer subjected to swift Xe ion irradiation"

Table S1. Crystallographic (experimental) data of HfO_2 (bulk material).

Space groups, classification code	Crystal parameters				Temperature, pressure
	a, b, c [nm], α, β, γ [°]	V [Å^3]	V/mol unit [Å^3]	Density [g/cm^3]	
Monoclinic, $P2_1/c$ (No14), 27313-ICSD [1]	0.511, 0.517, 0.529, 99.18 (β)	138.22	34.56	10.12	≤1600°C, ambient pressure
Monoclinic, $P2_1/c$ (No14), 638740-ICSD [2]	0.511, 0.517, 0.529, 99.0 (β)	137.9	34.48	10.14	≤1750°C, ambient pressure
Monoclinic, $P2_1/c$ (No14), 60902-ICSD [3]	0.511, 0.517, 0.529, 99.22 (β)	138.32	34.58	10.11	22 – 150°C, ambient pressure
Monoclinic, $P2_1/c$ (No14), 57385-ICSD [4]	0.5119, 0.5169, 0.5297, 99.18 (β)	138.36	34.59	10.10	25°C, ≤2.6GPa
Orthorhombic, Pbcm (No57), 53034-ICSD [5]	0.501, 0.523, 0.506	132.4	33.1	10.56	600°C, 6 GPa
Orthorhombic, Pbcm (No57), 638742-ICSD [4]	0.5054, 0.5270, 0.5115	136.24	34.06	10.26	Room temperature, 2.6 - 20 GPa
Orthorhombic, Pbca (No61), 79913-ICSD [6]	1.00, 0.523, 0.506	264.98	33.12	10.55	600°C, 6 GPa
Orthorhombic, Pnam (No62), 83863-ICSD [7]	0.555, 0.646, 0.331	118.61	29.65	11.79	25°C – 800°C 6 -13 GPa
Orthorhombic, Pmnb (No62), 87456-ICSD [8]	0.317, 0.541, 0.628	107.96	26.99	12.95	400°C 5 – 26 GPa
Tetragonal [9] *	0.514, 0.514, 0.525	138.70	34.67	-	1920±20°C, ambient pressure
Tetragonal, $P4_2/nmc$ (No137),7146-ICSD [10]	0.3647, 0.3647, 0.5329	70.89	35.44	9.86	2250 - 2450°C, ambient pressure
Cubic, $Fm\bar{3}m$, (No225) 53033-ICSD [11]	0.5125	134.61	33.65	10.39	>2500°C
Cubic, (No 225) ** Fm-3m [12]	0.53	148.88	-	10.40	2750°C-2900°C, ambient pressure

*No space group, atom positions were determined therefore is not present in ICSD.
**No atom positions were determined therefore is not present in ICSD.

[1] R. Ruh, P.W.R. Corfield, Crystal structure of monoclinic hafnia and comparison with monoclinic zirconia, J. Am. Cer. Soc. 53 (1970), pp. 126-129
[2] D.W. Stacy, J.K. Johnstone, D.R. Wilder, Axial thermal expansion of HfO_2, J. Am. Cer. Soc., 55 (1972), pp. 482-483
[3] R.E. Hann, P.R. Suitch, J.L. Pentecost, Monoclinic crystal structures of ZrO_2 and HfO_2 refined from X-ray powder diffraction data, J. Am. Cer. Soc. 68 (1985), pp. 285-286
[4] D.M. Adams, S. Leonard, D. R. Russell, R. J. Cernik, X-ray diffraction study of hafnia under high pressure using synchrotron radiation, J. Phys. Chem. Solids 52 (1991), pp. 1181-1186
[5] R. Suyama, H. Horiuchi, S. Kume, Structural refinement of ZrO_2 and HfO_2 treated at 600°C·6GPa, J. Ceram. Soc. Japan. 95 (1987), pp. 567-568.
[6] O. Ohtaka, T. Yamanaka, S. Kume, N. Hara, H. Asano, F. Izumi, Structure analysis of orthorhombic hafnia by neutron powder diffraction, J. Am. Cer. Soc. 78 (1995), pp. 233-237
[7] J. Haines, J.M. Leger, S. Hull, J.P. Petitet, A.S. Pereira, C.A. Perottoni, J.A.H. da Jornada, Characterization of the cotunnite-type phases of zirconia and hafnia by neutron diffraction and Raman spectroscopy, J. Am. Cer. Soc., 80 (1997), pp. 1910-1914
[8] J. Tang, M. Kai, Y. Kobayashi, S. Endo, O. Shimomura, T. Kikegawa, T. Ashida, A high-pressure high-temperature X-ray study of phase relations and polymorphism of HfO_2, Geophysical Monograph 101 (1998), pp. 401-407
[9] C. E. Curtis, M. Doney, J. R. Johnson, Properties of Hafnium Oxide, Hafnium Silicate, Calcium Hafnate, and Hafnium Carbide. J. Am. Ceram. Soc. 37(1954), pp. 458–65
[10] S. J. McCormack, R. J. Weber, W. M. Kriven, In-situ investigation of $Hf_6Ta_2O_{17}$ anisotropic thermal expansion and topotactic, peritectic transformation, Acta Mater. 161 (2018), pp. 127-137
[11] L. Passerini, Isoformismo tra ossidi di metalli tetravalenti. I sistemi: CeO_2 - ThO_2; CeO_2 - ZrO_2; CeO_2 - HfO_2, Gazzetta Chimica Italiana 60 (1930), pp. 762-776
[12] A. G. Boganov, V. S. Rudenko, L. P. Makarov, X-ray study of zirconium and hafnium dioxides at temperatures up to 2750◦ C, Dokl. Akad. Nauk SSSR, 160 (1965), pp. 1065–1068

Crystal phase identification.

Phase identification of HfO_2 by comparison between HRTEM micrographs and image simulation from JEMS.

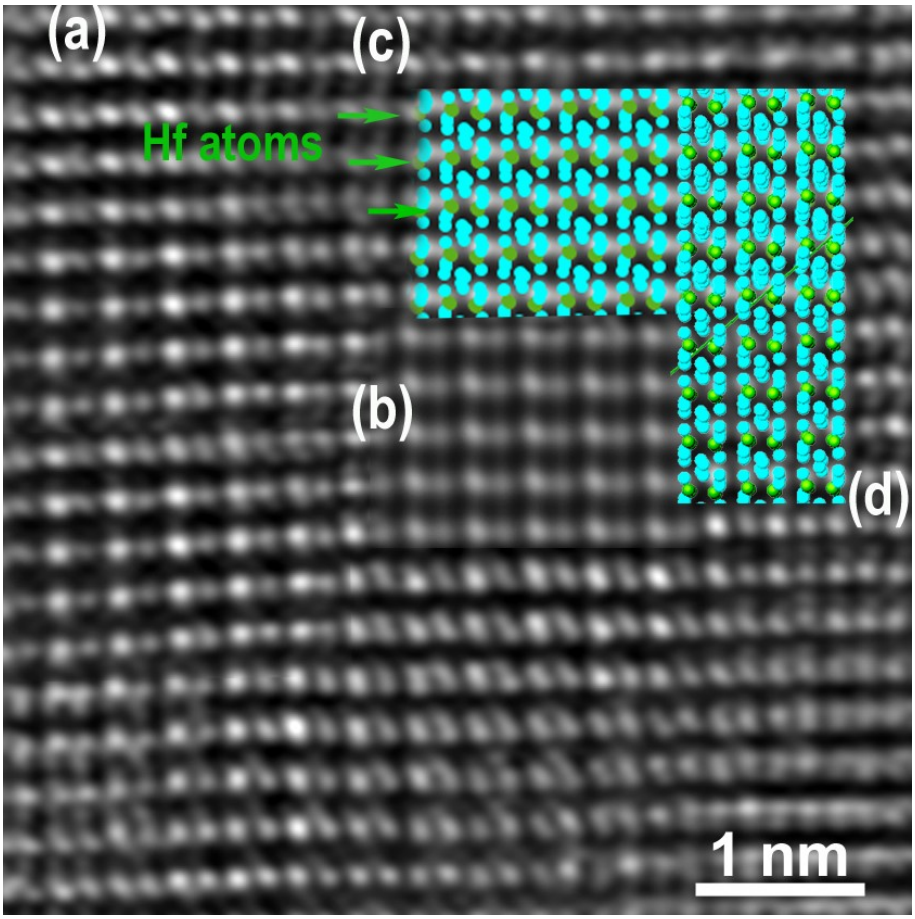

Figure S1. Pristine [112] HRTEM enlarged image from main text Figure 3 area.

(a) HRTEM image obtained along the [112] *Pbcm* HfO_2 direction;

(b) the inset is the HRTEM image simulation performed for the defocus value of 0 nm, assumed sample thickness of 43.5 nm, tilt out of [112] zone axis 1.78° with the Center of Laue Circle CLC at (4.760, 4,611, -4.686) close to the (55-5) reflection (HV 300 keV of accelerating voltage, spherical aberration *Cs*1.2 mm, chromatic aberration *Cc*1.1 mm);

(c) the inset is the HRTEM image simulation with Hf and O atoms superimposed onto the simulated image, arrows indicate the positions of Hf atoms;

(d) the inset is the HfO_2 structural model along the [112] direction.

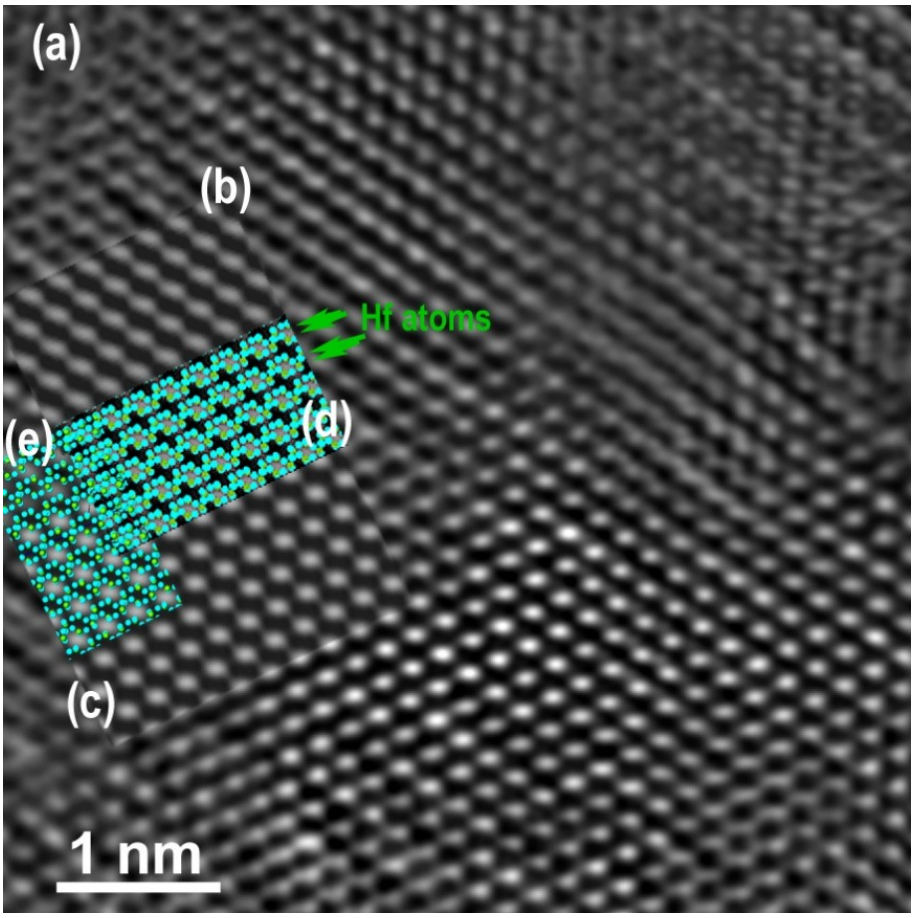

Figure S2. Pristine [111] HRTEM enlarged image from main text Figure 3

(a) HRTEM image obtained along the [111] *Pbcm* HfO_2 direction;

(b) the inset is the HRTEM image simulation performed for a 6 nm defocus and assuming a 40.6 nm sample thickness (HV 300 keV of accelerating voltage, *Cs*1.2 mm, *Cc*1.1 mm);

(c) the inset is the HRTEM image simulation with Hf and O atoms superimposed onto the simulated image, arrows indicate the positions of Hf atoms;

(d) the inset is the HfO_2 structural model along the [111] direction superimposed with the simulated and the experimental HRTEM images.

HRTEM simulation with JEMS for phase identification in irradiated with 160 MeV Xe ions La:HfO2 with tetragonal *P4₂/nmc* structure

The enlarge HRTEM image for Figure 4 in the main text.

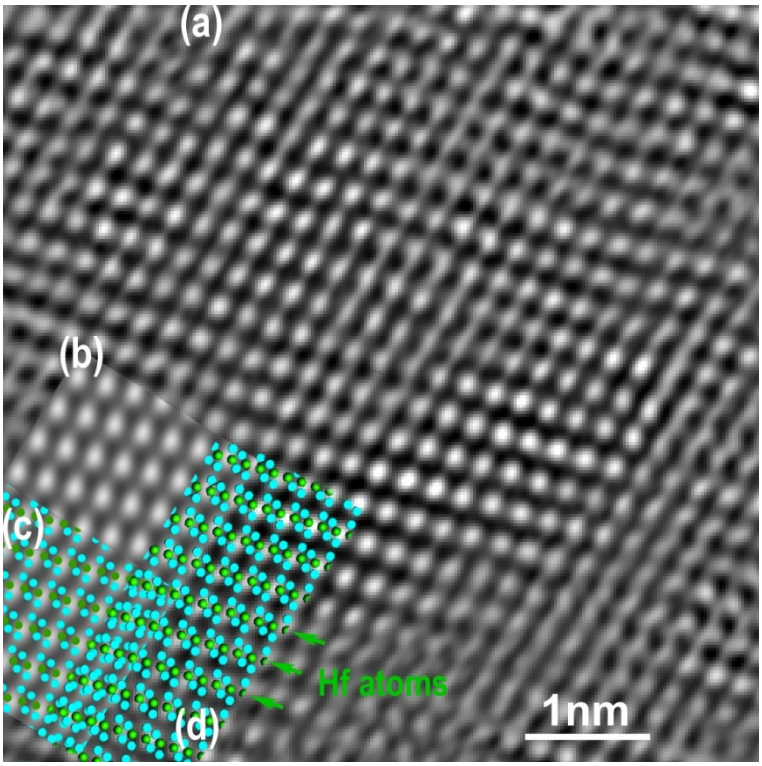

Figure S3. [1-21] HRTEM image from 160 MeV Xe ion irradiated sample, enlarged from main text Figure 4

(a) HRTEM image obtained along the [1-21] *P4₂/nmc* HfO_2 direction;

(b) the inset is the HRTEM image simulation performed for a 30 nm defocus and assuming a 55.53 nm sample thickness (HV 200 keV of accelerating voltage, *Cs*1.2 mm, *Cc*1.1 mm);

(c) the inset is the HRTEM image simulation with Hf and O atoms superimposed onto the simulated image, arrows indicate the positions of Hf atoms;

(d) the inset is the HfO_2 structural model along the [1-21] direction superimposed with the simulated and the experimental HRTEM images.

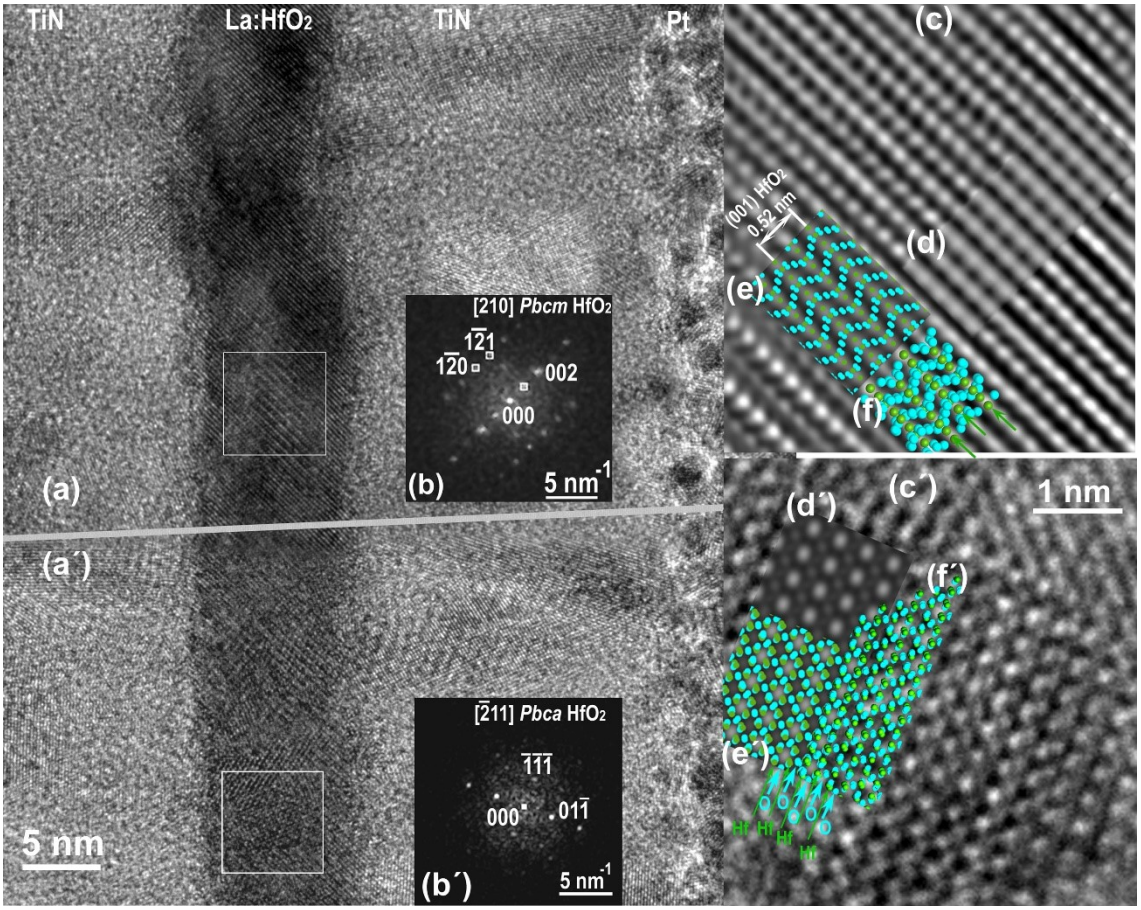

Figure S4. HRTEM images from Xe 24 MeV irradiated sample,

(a) and (a′): HRTEM images of the La:HfO_2 layer irradiated with 24 MeV Xe ions,

b: FFT from the adjacent 6.5 nm x 6.5 nm area matching the simulation of orthorhombic [210] *Pbcm* HfO_2;

(c): enlarged HRTEM image filtered with (-1-1-1) and (01-1) reflections,

(d, e, and f): insets for HfO_2 orthorhombic *Pbcm* [210]: simulated HRTEM image, simulated HRTEM image with superimposed Hf and O atoms (defocus 85 nm, estimated sample thickness of 53 nm, HV 200 keV, *Cs*1.2 mm, *Cc*1.1 mm) and structural model of [210] HfO_2 orth *Pbcm*;

(b′): FFT from the 6.5 nm x 6.5 nm adjacent area matching the simulation of orthorhombic [-211] *Pbca* HfO_2;

(c′): enlarged filtered HRTEM image of [-211] *Pbcm* orthorhombic HfO_2 from the selected area,

(d′, e′ and f′): insets for HfO_2 orthorhombic *Pbcm* [-211]: simulated HRTEM image, simulated HRTEM image with superimposed Hf and O atoms (defocus 85 nm, estimated sample thickness of 47 nm, HV 200 keV, *Cs*1.2 mm, *Cc*1.1 mm) and structural model of [-211] HfO_2 orth *Pbca.*